Scripta Materialia 162 (2019) 176–180

Contents lists available at ScienceDirect

Scripta Materialia

journal homepage: www.elsevier.com/locate/scriptamat

Finite temperature elastic properties of equiatomic CoCrFeNi from first principles

Yifeng Wu, Douglas L. Irving*

Department of Materials Science and Engineering, North Carolina State University, Raleigh, NC 27695, USA

ARTICLE INFO

Article history:
Received 12 October 2018
Accepted 2 November 2018
Available online xxxx

Keywords:
Metal and alloys
Elastic behavior
Spin fluctuations
First-principle calculation
Density functional theory (DFT)

ABSTRACT

The finite temperature elastic properties of the equiatomic CoCrFeNi medium-entropy alloy has been studied by density functional theory. Besides atomic vibrations and electronic free energy, the predictive model developed here includes contributions from spin fluctuations (SFs) in determining the elastic properties of CoCrFeNi. Including SFs changes the magnitude of the temperature derivatives of the poly-crystal elastic moduli, resulting in a close agreement between simulation and experimentally measured trends. How the single-crystal elastic moduli depend on SFs and how these dependencies influence changes in the poly-crystal elastic moduli are analyzed systematically. Finally, the elemental sources to the simulated trends are identified.

High-entropy alloys (HEAs) are an exciting class of materials that were independently discovered by Yeh and Cantor et al. [1,2] HEAs consist of five or more components in equiatomic or near-equiatomic composition, and form as random solid solution (RSSs) on simple lattice structures (fcc, bcc or hcp), which has been attributed, in part, to the excessive configurational entropy that results from the number of components and composition. Beyond the many reported properties of HEAs, their discovery inspired the search over wider phase spaces for alloy design than previously considered and deviated from conventional rules of thumb that tend to avoid the center of the multi-component phase diagram. This has also extended to explorations of the center of the phase diagram of ternary and quaternary equiatomic alloys [3,4], which are now being referred to either by their entropy (medium or low) or more broadly as compositionally complex alloys (CCAs) [5].

HEAs and CCAs have garnered significant attention because of an excellent combination of mechanical properties [6]. Otto et al. [7] recently demonstrated that the plastic deformation mechanism of an equiatomic CoCrFeMnNi HEA switched from dislocation motion to nanoscale twinning when it approached cryogenic temperatures, resulting in a substantial increase of both strength and ductility. Xia et al. [8] reported that Al_xCoCrFeNi HEAs exhibited advanced irradiation resistance, which was attributed to a self-healing process where the material cycled between amorphization and crystallization to recover from defect accumulations; a capability that makes HEAs promising candidates for next-generation nuclear reactors. Low-density HEAs have also demonstrated unique combinations of high hardness while retaining some residual ductility [9].

There has also been theoretical progress aimed at developing an atomic-level understanding of the relationship between the structure of the HEAs and their macroscale properties. Varvenne et al. recently developed a strengthening theory for fcc HEAs, where the variety of local chemical potentials induced a distorted dislocation configuration, impeding the dislocation motion [10]. While local crystal basis distortions have been found to be small in CoCrFeMnNi-based systems, they were recently characterized and predicted to contribute considerably to the ground-state lattice parameters and bulk moduli of bcc refractory HEAs where the elemental atomic radii differed more substantially [11,12]. The influence of local magnetic moments in these multi-component random alloys has also been studied and shown to be important to short-range chemical ordering and predicted thermodynamics [13,14].

The equiatomic CoCrFeNi medium-entropy alloy (MEA) is a critical base alloy for many HEAs of interest [15-19]. Its properties are

* Corresponding author.
E-mail address: dlirving@ncsu.com (D.L. Irving).

https://doi.org/10.1016/j.scriptamat.2018.11.010
1359-6462/

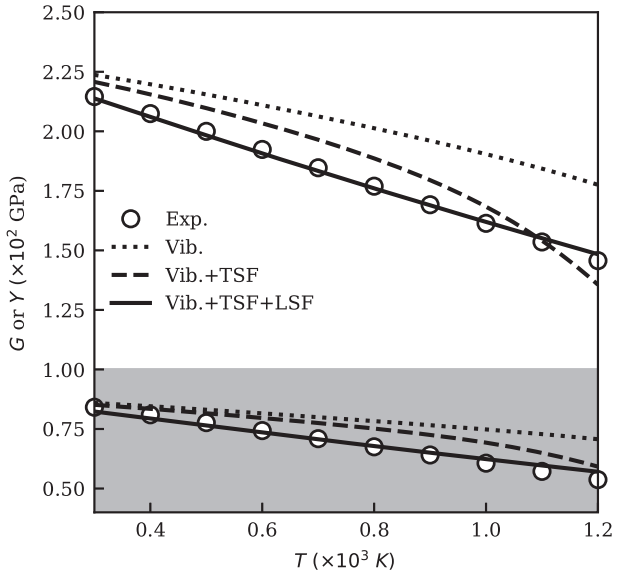

Fig. 1. Simulated and experimental [40] shear modulus G and Young's modulus Y of the homogenized poly-crystal CoCrFeNi MEA as a function of temperature. G and Y are marked by the shaded and unshaded areas, respectively.

thus important to the design of these alloys while at the same time being slightly less computationally demanding to address. In the elemental solids of the components making up this alloy, the local magnetic moments of Cr, Fe and Ni are known to persist at temperatures well above the Curie point even in the paramagnetic state [20-22]. Because of this and a Curie point at 120 K [13,23], substantial spin fluctuations (SFs) are possible in CoCrFeNi above room temperature. These fluctuations may play a significant role in the free energy of the alloy and its dependence on strain and, thus, properties that depend on this free energy landscape.

At finite temperatures, besides transverse spin fluctuation (TSF), longitudinal spin fluctuation (LSF) also takes place [24]. In stainless steels, Vitos and Johansson [25] found that the LSF contributions to the temperature dependencies of the single-crystal elastic moduli are comparable to those of anharmonic effects. The stacking-fault energies of stainless steels were later shown to be dominated by LSFs within an extensive temperature range, indicating a large evidence of magnetostructural behavior [26-28].

Using first-principles approaches, the elastic properties of CoCrFeNi were explored as a function of temperature by considering SFs (TSF and LSF) as well as atomic vibrations and electronic free energy. It shows that the inclusion of SFs leads to capturing the experimentally measured trends of the poly-crystal elastic moduli as a function of temperature. The inclusion of SFs changes the free energy surface landscape, its temperature and strain dependencies, and, ultimately, the properties dependent on this surface. This is found to manifest itself in changes to the magnitude of the temperature derivatives of single crystal and poly-crystal elastic moduli. Finally, the elemental sources that make the most significant contributions to the simulated trends are identified for this MEA. While the focus is on elastic properties, this also has implications for other mechanical properties, such as the ideal tensile and shear strengths [29] that also depend on the free energy landscape.

All the calculations were performed on an fcc primitive cell with the Exact Muffin-Tin Orbitals (EMTO) theory [30-32]. The chemical and magnetic disorders were treated by Coherent Potential Approximation (CPA) [33] and Disordered Local Moment (DLM) [34], respectively. The Green's functions were calculated for 16 complex energy points with the basis set including s, p, d, and f states. The Screened Impurity Model (SIM) parameter was set to 0.9 for the electrostatic correction to the single-site CPA. A 13 × 13 × 13 k-point mesh for reciprocal-space integration was selected to ensure the numerical error below 1 meV/atom.

The Helmholtz free energy per atomic formula $F(\Omega, T)$ is a sum of the magnetic free energy $F_{\text{mag}}(\Omega, [M_i], T)$, the vibrational free energy $F_{\text{vib}}(\Omega, [M_i], T)$ and the electronic free energy $F_{\text{ele}}(\Omega, [M_i], T)$ [25,35]. Specifically, F_{mag} was treated here as $E_{\text{int}}(\Omega, [M_i]) - TS_{\text{mag}}([M_i])$ with E_{int} being the internal energy that depends on atomic volume Ω and a set of local magnetic moments of individual species $[M_i]$, S_{mag} the magnetic entropy treated by a mean-field approximation for fully random configurations [21]: $S_{\text{mag}} = k_B \sum_i x_i \ln(|M_i| + 1)$ with k_B denoting the Boltzmann constant and x_i the bulk number density of i. F_{vib} was evaluated by the Debye model [36], where the elastic Debye temperature Θ_D was calculated via the mean velocity of single-crystal sound waves according Refs. [32,37]. To compare the simulated and experimental poly-crystal shear modulus G and Young's modulus Y, the Voigt-Reuss-Hill (VRH) averages [38] of C' and C_{44} were adopted. C' and C_{44} were calculated as a function of Ω and $[M_i]$ through the volume-conserved orthorhombic and monoclinic distortions, respectively [32]. For F_{ele}, the Fermi distribution function was used as done by Wang et al. [39] At a given temperature, the Helmholtz free energy at each volume was minimized as a function of $[M_i]$.

Results from the above approach will now be compared to experimental measurements. At low temperatures, the model slightly overestimates the values of G and Y for the alloy as compared to the low-temperature experimental measurements from Laplanche et al. [40]. There is a constant deviation of approximately 10 GPa for G throughout the whole temperature range. From an *ab initio* perspective, this is not a significant magnitude since a 1% increase of the lattice constant results in a 5 to 10 GPa reduction of G. To test this assertion, the room-temperature elastic properties of the alloy were determined by forcing the lattice constant to be the experimental value of 3.57 Å. In doing this, the experimental measured results were reproduced perfectly where G and Y equal to 86 GPa and 214 GPa, respectively. The same is accomplished by shifting G down by 10 GPa, which is done for all future comparisons between the theoretical and experimental G and Y as a function of temperature.

Three submodels are compared to experimental trends as a function of temperature: the first submodel only includes the vibrational contributions (Vib.), the second includes vibration and TSF (Vib.+TSF), while the third includes all factors (Vib.+TSF+LSF). The electronic free energy contributions are also included in all three submodels and their omission leads to only small changes in the presented trends. These are presented in Fig. 1. Including only vibration leads to a decrease in G and Y with temperature that is generally offset from experiment but the rate of change is lower than the experiment, which leads to larger differences at higher temperatures. Adding TSFs with magnetic moments fixed at their 0 K levels results in a slight improvement over the previous submodel, but

Table 1
Average (300–600 K) temperature derivatives of B, C', C_{44}, G and Y (in 10^{-2} GPa/K) and average values of α and β within the three submodels.

	$\frac{\partial B}{\partial T}$	$\frac{\partial C'}{\partial T}$	$\frac{\partial C_{44}}{\partial T}$	α	β	$\frac{\partial G}{\partial T}$	$\frac{\partial Y}{\partial T}$
Vib.	−5.5	−0.7	−2.4	3.8	2.0	−1.4	−4.2
Vib.+TSF	−8.7	−0.8	−3.1	3.8	1.9	−1.8	−5.8
Vib.+TSF+LSF	−6.6	−1.7	−4.0	4.1	1.9	−2.9	−7.7

Table 2
Average (300–600 K) anharmonic and constant volume components of the temperature derivatives of C' and C_{44} (in 10^{-2} GPa/K) within the three submodels.

	$\left(\frac{\partial C'}{\partial T}\right)_{ah}$	$\left(\frac{\partial C'}{\partial T}\right)_{cv}$	$\left(\frac{\partial C_{44}}{\partial T}\right)_{ah}$	$\left(\frac{\partial C_{44}}{\partial T}\right)_{cv}$
Vib.	−0.7		−2.4	
Vib.+TSF	−0.8		−3.1	
Vib.+TSF+LSF	−1.0	−0.7	−3.5	−0.5

significant deviations and non-linearity at high temperatures are evident, which are caused by the divergence of thermal expansion predicted by this submodel. The Vib.+TSF+LSF submodel has a rate of change in moduli with temperature that is in close agreement with experimental measurements and it also does not have the offset in moduli that is present in the other submodels. Clearly, the inclusion of SFs, especially LSFs, is important in capturing the changes of G and Y as a function of temperature.

To explore the underlying mechanism of how SFs influence the poly-crystal elastic moduli, the single-crystal elastic moduli C' and C_{44} need to be investigated due to a direct correlation with G and Y by the aforementioned VRH average [38]. The temperature derivatives of G and Y from the VRH average are given in Eq. (1):

$$\frac{\partial G}{\partial T} = \left[\frac{1}{5} + \frac{5\alpha^2}{(2\alpha+3)^2}\right]\frac{\partial C'}{\partial T} + \left[\frac{3}{10} + \frac{15/2}{(2\alpha+3)^2}\right]\frac{\partial C_{44}}{\partial T},$$
$$\frac{\partial Y}{\partial T} = \frac{9}{(3\beta+1)^2}\frac{\partial B}{\partial T} + \frac{27\beta^2}{(3\beta+1)^2}\frac{\partial G}{\partial T}. \quad (1)$$

In these equations, the dimensionless variables α and β signify C_{44}/C' and B/G (the Pugh's ratio [41]), respectively. Moreover, α and β were found to be largely insensitive to temperature and submodel in the simulations. Therefore, the temperature derivatives of G and Y are proportional to those of C' and C_{44}. It is found that both C' and C_{44} decrease linearly with the temperature and, thus, their temperature derivatives remain constant as T increases. The exception to this is the high-temperature non-linearity in the Vib.+TSF submodel above 600 K, but even this submodel is fairly linear in the lower temperature limit (300–600 K). Hence, $\partial G/\partial T$ and $\partial Y/\partial T$ are solely dependent on $\partial B/\partial T$, $\partial C'/\partial T$ and $\partial C_{44}/\partial T$ and how those variables depend on SFs.

The average temperature derivatives of B, C', and C_{44} and the average values of α and β within 300–600 K are listed in Table 1, along with those of G and Y calculated by Eq. (1). Comparing the Vib. submodel to the Vib.+TSF+LSF submodel, all the derivatives are increasingly negative in the latter. This leads to a larger decrease with temperature for this submodel. The influence of LSFs induces increasingly negative temperature derivatives of C' and C_{44} as compared to the submodel that only includes TSFs. Although $\partial B/\partial T$ is more negative without LSFs, $\partial Y/\partial T$ is dominated by $\partial G/\partial T$ through $\partial C'/\partial T$ and $\partial C_{44}/\partial T$. As a result, the more negative $\partial B/\partial T$ has a less significant impact in the observed trends with temperature.

To further explore why the larger magnitudes of the temperature derivatives of C' and C_{44} arise when LSFs are included each single crystal elastic coefficient was separated into a constant temperature (anharmonic) and a constant volume contributions (Table 2). The former is induced by thermal expansion that results from atomic vibrations, SFs, and electronic free energy, as well as their coupling.

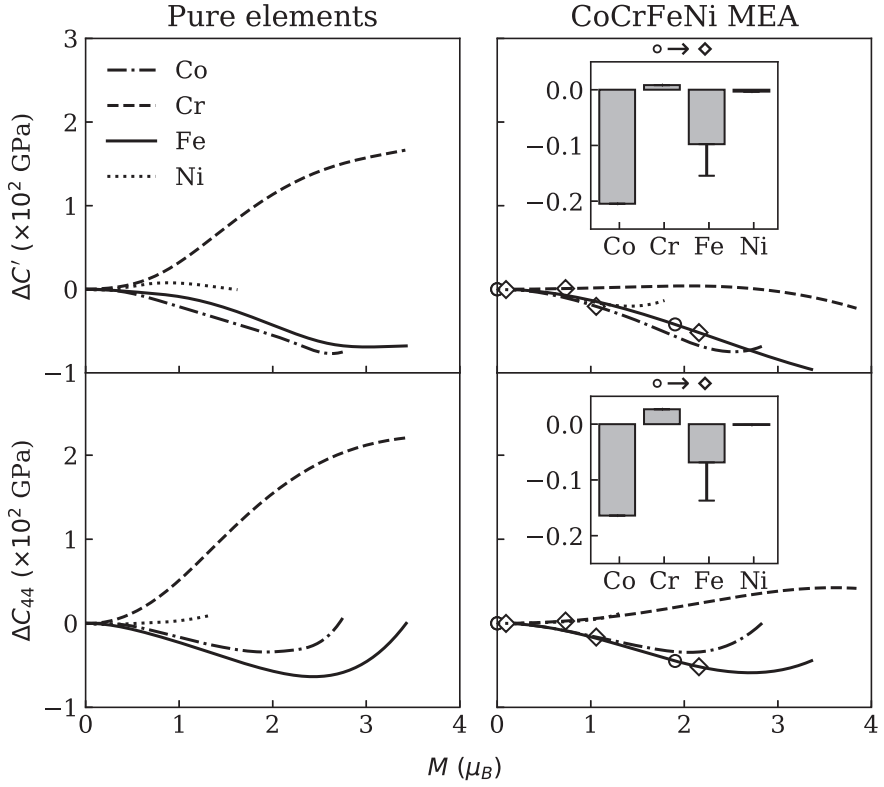

Fig. 2. Changes in C' and C_{44} of the pure elements and CoCrFeNi as a function of on-site magnetic moments. Equilibrium states for each element at 0 K and 1200 K are represented by open circle and diamond, respectively. Specific contributions from individual elements when T goes from 0 K to 1200 K are shown in the inset plots, where the error bars indicate the differences between the Fe contributions in $Fe_{70}Cr_{15}Ni_{15}$ [25] and CoCrFeNi. All the y-axis values are normalized by the chemical compositions.

Table 3
Average (300–600 K) anharmonic and constant volume components of the temperature derivatives of C' and C_{44} (in 10^{-2} GPa/K) in $Fe_{70}Cr_{15}Ni_{15}$ [25] and CoCrFeNi.

	$\left(\frac{\partial C'}{\partial T}\right)_{ah}$	$\left(\frac{\partial C'}{\partial T}\right)_{cv}$	$\left(\frac{\partial C_{44}}{\partial T}\right)_{ah}$	$\left(\frac{\partial C_{44}}{\partial T}\right)_{cv}$
$Fe_{70}Cr_{15}Ni_{15}$	−1.0	−0.9	−3.2	−0.8
CoCrFeNi	−1.0	−0.7	−3.5	−0.5

The latter comes solely from the LSFs. A similar analysis was performed by Huang et al. [42] and the resulting separation is given in Eq. (2):

$$\begin{aligned}\Delta C(T) &\equiv C(V,T) - C(V_0,T_0)\\ &= C(V,T) - C(V_0,T) + C(V_0,T) - C(V_0,T_0)\\ &= \Delta C(T)_{ah} + \Delta C(T)_{cv},\end{aligned} \tag{2}$$

In this expression, C is a dummy variable representing either C' or C_{44}, the subscripts ah and cv stand for anharmonic and constant volume, respectively. Here, $C(V_0,T_0)$ is the 0 K value of C. The anharmonic and constant volume components of $\partial C'/\partial T$ and $\partial C_{44}/\partial T$ of the MEA within the three submodels are presented in Table 1. Incorporating TSFs, the magnitude of anharmonic contribution to $\partial C'/\partial T$ increases slightly, while that to $\partial C_{44}/\partial T$ shows a more significant increase in magnitude. Additional gain in the anharmonic contribution is observed for each elastic constant with the inclusion of LSFs.

The larger anharmonic contribution by including SFs was found to be associated with a substantial increase of thermal expansion coefficient (TEC). To illustrate this, the average (300–600 K) instantaneous TEC was calculated, which shows an increase from 16.6 to 27.5 (in $\times 10^{-6}$/K) with the inclusion of SFs. Addition of LSFs slightly increases the instantaneous TEC. The above is related to the fact that larger magnetic moments are favored in larger volumes, which leads to an increased magnetic entropy (free energy is reduced) and, thus, an increased TEC.

The constant volume component consists of individual elemental sources. To distinguish them, C' and C_{44} are shown in Fig. 2 as a function of the on-site magnetic moments for each individual element at the ground-state volume. While one moment is varied in the alloy, all other moments are set to zero. For a guideline to the rich limit of each species, similar DLM calculations for pure elements in the same lattice geometry were also performed. As illustrated in Fig. 2, the general trends of $\partial C'/\partial M_i$ and $\partial C_{44}/\partial M_i$ are similar when comparing trends in the alloy to those in the elemental phases. In the pure elements, C' increases with M_{Cr} while it decreases with all the other elements. C_{44} was found to increase with both M_{Cr} and M_{Ni} while it decreases with M_{Co} and M_{Fe}. In the MEA, the above trends hold but the contributions from Cr are suppressed substantially, and both C' and C_{44} display only a weak increase and nearly a plateau with M_{Cr}, especially the former.

To show the differences between the current MEA and conventional alloys, Table 3 presents comparisons with those of a $Fe_{70}Cr_{15}Ni_{15}$ austenitic steel [25]. The anharmonic contributions to $\partial C'/\partial T$ are identical in both alloys, while that to $\partial C_{44}/\partial T$ in the MEA is more negative by -0.3×10^{-2} GPa/K. The constant volume components for both C' and C_{44} of the MEA are less pronounced than those in the steel. The inset plots of Fig. 2 give the specific contributions from individual elements with temperature changing from 0 K to 1200 K. For both C' and C_{44}, the temperature-induced reductions are predominately from the LSFs of Co, followed by those of Fe, while those of Cr and Ni are nearly trivial. The differences between the Fe contributions in the MEA and those in $Fe_{70}Cr_{15}Ni_{15}$ are manifested by the error bars. Obviously, the Fe contribution in the MEA is much lower than that in the steel, indicating a suppression of the LSFs of Fe in the MEA by the large chemical chaos. Due to the equiatomic composition, the Co contribution appears to make up for the suppression of the Fe contribution in the MEA as compared to the steel, but the overall constant volume components of the temperature derivatives of C' and C_{44} are still less negative than those in the steel.

Using first principles simulation we have explored the importance of SFs in predicting the finite temperature elastic properties of CoCrFeNi. While inclusion of all factors are important to predicting the elastic properties of this equiatomic alloy, the results also suggest that SFs may also be important in predicting the properties of CCAs with off-stoichiometric compositions in systems that sustain finite magnetic moments above the Curie temperature.

Acknowledgment

The authors gratefully acknowledge the financial support from the National Science Foundation from grant DMR-1151568 for work on this effort.

References

[1] J. Yeh, S. Chen, S. Lin, J. Gan, T. Chin, T. Shun, C. Tsau, S. Chang, Adv. Eng. Mater. 6 (5) (2004) 299–303. https://doi.org/10.1002/adem.200300567.
[2] B. Cantor, I. Chang, P. Knight, A. Vincent, Mater. Sci. Eng. A 375 (2004) 213–218. https://doi.org/10.1016/j.msea.2003.10.257.
[3] C. Niu, A. Zaddach, C. Koch, D. Irving, J. Alloys Compd. 672 (2016) 510–520. https://doi.org/10.1016/j.jallcom.2016.02.108.
[4] J. Miao, C. Slone, T. Smith, C. Niu, H. Bei, M. Ghazisaeidi, G. Pharr, M. Mills, Acta Mater. 132 (2017) 35–48. https://doi.org/10.1016/j.actamat.2017.04.033.
[5] D. Miracle, O. Senkov, Acta Mater. 122 (2017) 448–511. https://doi.org/10.1016/j.actamat.2016.08.081.
[6] H. Diao, X. Xie, F. Sun, K. Dahmen, P. Liaw, Mechanical Properties of High-entropy Alloys, ch. 6. Springer. 2016, 181–236. https://doi.org/10.1007/978-3-319-27013-5_6.
[7] F. Otto, A. Dlouhỳ, C. Somsen, H. Bei, G. Eggeler, E. George, Acta Mater. 61 (15) (2013) 5743–5755. https://doi.org/10.1016/j.actamat.2013.06.018.
[8] S. Xia, Z. Wang, T. Yang, Y. Zhang, J. Iron Steel Res. Int. 22 (2015) 879–884. https://doi.org/10.1016/S1006-706X(15)30084-4.
[9] K.M. Youssef, A.J. Zaddach, C. Niu, D.L. Irving, C.C. Koch, Mater. Res. Lett. 3 (2) (2015) 95–99. https://doi.org/10.1080/21663831.2014.985855.
[10] C. Varvenne, A. Luque, W. Curtin, Acta Mater. 118 (2016) 164–176. https://doi.org/10.1016/j.actamat.2016.07.040.
[11] H. Song, F. Tian, Q. Hu, L. Vitos, Y. Wang, J. Shen, N. Chen, Phys. Rev. Mater. 1 (2) (2017) 023404. https://doi.org/10.1103/PhysRevMaterials.1.023404.
[12] L. Tian, G. Wang, S. Joshua, D. Irving, J. Zhao, L. Vitos, Mater. Des. 114 (2017) 243–252. https://doi.org/10.1016/j.matdes.2016.11.079.
[13] C. Niu, A. Zaddach, A. Oni, X. Sang, J.H. III, J. LeBeau, C. Koch, D. Irving, Appl. Phys. Lett. 106 (16) (2015) 161906. https://doi.org/10.1063/1.4918996.
[14] D. Ma, B. Grabowski, F. Körmann, J. Neugebauer, D. Raabe, Acta Mater. 100 (2015) 90–97. https://doi.org/10.1016/j.actamat.2015.08.050.
[15] Y. Kao, T. Chen, S. Chen, J. Yeh, J. Alloys Compd. 488 (1) (2009) 57–64. https://doi.org/10.1016/j.jallcom.2009.08.090.
[16] C. Tung, J. Yeh, T. Shun, S. Chen, Y. Huang, H. Chen, Mater. Lett. 61 (1) (2007) 1–5. https://doi.org/10.1016/j.matlet.2006.03.140.
[17] A. Zaddach, C. Niu, C. Koch, D. Irving, Jom 65 (12) (2013) 1780–1789. https://doi.org/10.1007/s11837-013-0771-4.
[18] A. Zaddach, C. Niu, A. Oni, M. Fan, J. LeBeau, D. Irving, C. Koch, Intermetallics 68 (2016) 107–112. https://doi.org/10.1016/j.intermet.2015.09.009.
[19] H. Zhang, Y. Pan, Y. He, Mater. Des. 32 (4) (2011) 1910–1915. https://doi.org/10.1016/j.matdes.2010.12.001.
[20] G. Grimvall, J. Häglund, A. Guillermet, Phys. Rev. B 47 (22) (1993) 15338. https://doi.org/10.1103/PhysRevB.47.15338.
[21] G. Grimvall, Phys. Rev. B 39 (16) (1989) 12300. https://doi.org/10.1103/PhysRevB.39.12300.
[22] O. Steinsvoll, C. Majkrzak, G. Shirane, J. Wicksted, Phys. Rev. Lett. 51 (4) (1983) 300. https://doi.org/10.1103/PhysRevLett.51.300.
[23] M. Lucas, L. Mauger, J. Munoz, Y. Xiao, A. Sheets, S. Semiatin, J. Horwath, Z. Turgut, J. Appl. Phys. 109 (7) (2011) 07E307. https://doi.org/10.1063/1.3538936.
[24] S. Shallcross, A.E. Kissavos, V. Meded, A. Ruban, Phys. Rev. B 72 (10) (2005) 104437. https://doi.org/10.1103/PhysRevB.72.104437.
[25] L. Vitos, B. Johansson, Phys. Rev. B 79 (2) (2009) 024415. https://doi.org/10.1103/PhysRevB.79.024415.
[26] L. Vitos, P. Korzhavyi, B. Johansson, Phys. Rev. Lett. 96 (11) (2006) 117210. https://doi.org/10.1103/PhysRevLett.96.117210.
[27] L. Vitos, P. Korzhavyi, J. Nilsson, B. Johansson, Phys. Scr. 77 (6) (2008) 065703. http://stacks.iop.org/1402-4896/77/i=6/a=065703.

[28] L. Vitos, J. Nilsson, B. Johansson, Acta Mater. 54 (14) (2006) 3821–3826. https://doi.org/10.1016/j.actamat.2006.04.013.
[29] X. Li, S. Schönecker, W. Li, L.K. Varga, D.L. Irving, L. Vitos, Phys. Rev. B 97 (9) (2018) 094102. https://doi.org/10.1103/PhysRevB.97.094102.
[30] L. Vitos, H. Skriver, B. Johansson, J. Kollár, Comput. Mater. Sci. 18 (1) (2000) 24–38. https://doi.org/10.1016/S0927-0256(99)00098-1.
[31] L. Vitos, Phys. Rev. B 64 (1) (2001) 014107. https://doi.org/10.1103/PhysRevB.64.014107.
[32] L. Vitos, Computational Quantum Mechanics for Materials Engineers: The EMTO Method and Applications, Springer Science & Business Media. 2007. https://doi.org/10.1007/978-1-84628-951-4.
[33] B. Gyorffy, Phys. Rev. B 5 (6) (1972) 2382. https://doi.org/10.1103/PhysRevB.5.2382.
[34] B. Gyorffy, A. Pindor, J. Staunton, G. Stocks, H. Winter, J. Phys. F 15 (6) (1985) 1337. http://stacks.iop.org/0305-4608/15/i=6/a=018.
[35] Z. Dong, W. Li, D. Chen, S. Schönecker, M. Long, L. Vitos, Phys. Rev. B 95 (5) (2017) 054426. https://doi.org/10.1103/PhysRevB.95.054426.
[36] V. Moruzzi, J. Janak, K. Schwarz, Phys. Rev. B 37 (2) (1988) 790. https://doi.org/10.1103/PhysRevB.37.790.
[37] G. Grimvall, Some Relations for Harmonic Lattice Vibrations, ch. Appendix D. Elsevier. 1999, 362–364. https://doi.org/10.1016/B978-044482794-4/50024-3.
[38] R. Hill, Proc. Phys. Soc. Sect. A 65 (5) (1952) 349. http://stacks.iop.org/0370-1298/65/i=5/a=307.
[39] Y. Wang, J. Wang, H. Zhang, V. Manga, S. Shang, L. Chen, Z. Liu, J. Phys. Condens. Matter 22 (22) (2010) 225404. http://stacks.iop.org/0953-8984/22/i=22/a=225404.
[40] G. Laplanche, P. Gadaud, C. Bärsch, K. Demtröder, C. Reinhart, J. Schreuer, E. George, J. Alloys Compd. 746 (2018) 244–255. https://doi.org/10.1016/j.jallcom.2018.02.251.
[41] S. Pugh, Lond. Edinb. Dublin Philos. Mag. J. Sci. 45 (367) (1954) 823–843. https://doi.org/10.1080/14786440808520496.
[42] L. Huang, L. Vitos, S. Kwon, B. Johansson, R. Ahuja, Phys. Rev. B 73 (10) (2006) 104203. https://doi.org/10.1103/PhysRevB.73.104203.